Numerical Simulations on Flow Characteristics of a Nozzle-Flapper Servo Valve With Diamond Nozzles

HE YANG[ID], WEN WANG, AND KEQING LU

School of Mechanical Engineering, Hangzhou Dianzi University, Hangzhou 310018, China

Corresponding author: He Yang (yanghe@hdu.edu.cn)

ABSTRACT Nozzle-flapper servo valves are widely used in modern electro-hydraulic control systems of many engineering applications. Flow cavitation in the nozzle-flapper pilot stage could produce noise and cavitation erosion, reducing the performance stability and reliability of the servo valves. In this paper, diamond nozzles are proposed to replace the traditional circular nozzles to reduce the flow cavitation in the nozzle-flapper stage. Numerical simulations using CFD software ANSYS/FLUENT were conducted to explore the flow characteristics of the nozzle-flapper pilot stage. Mass flow rate and image measurements were performed to verify the simulation results. Vapor fraction, lateral velocity, pressure distribution, and flow force are compared in detail between the pilot stage with the traditional nozzles and with the diamond nozzles. It is found that the vapor fraction is greatly reduced under the effect of the diamond nozzles. Finally, to explore the effect of the diamond nozzles on the performance of the nozzle-flapper servo valve, the pressure-flow characteristics and time step response of the load flow rate are examined using the software AMESim. The simulation results show that the pressure-flow characteristics and time step response of the load flow rate almost remain the same. This suggests that the diamond nozzles could suppress the cavitation in the nozzle-flapper servo valve without varying its performance.

INDEX TERMS Hydraulic valve, servo valve, cavitation reduction, flow force, CFD modeling, AMESim simulation.

I. INTRODUCTION

Since hydraulic control systems can produce fast linear movement and large forces, they are widely used in many engineering applications, such as robotic manipulators, flight wing control, and many heavy machineries [1], [2]. As the key component of the hydraulic control systems, hydraulic servo valve determines the stability, reliability and output of the hydraulic systems [3], [4]. A two-stage nozzle-flapper servo valve consists of the nozzle-flapper pilot stage and the spool stage. The former one converts the electronical signal to the flow pressure, which further drive the spool to move. Thus, the flow characteristics in the nozzle-flapper stage are crucial to the accurate spool movement and consequently the hydraulic output of the servo valve.

Flow cavitation is one of the key issues that may lead to pressure fluctuations, noise and cavitation erosion in the

hydraulic control systems. Considerable interest has been given to cavitation suppression of the hydraulic valves. Amirante et al. [5] conducted numerical and experimental investigations on the cavitation of the hydraulic proportional directional valves and found that flow cavitation becomes intensified over the metering conical surfaces. They proposed that the cavitation suppression may be achieved by removing the metering conical surfaces. Zou et al. [6] investigated the flow cavitation in the spool valve with non-circular openings and U-shaped grooves and found that the cavitation becomes more serious with the increase of valve opening and groove depth. Flow cavitation in the water hydraulic systems is more violent than that in the oil counterparts. Han et al. [7] found that the increase in the cone angle could intensify the flow cavitation in water hydraulic poppet valves while the increase in the back pressure could reduce the flow cavitation. Liang et al. [8] found that flow cavitation could be suppressed by the employment of the grooves at the port of the water hydraulic poppet valves.

The associate editor coordinating the review of this manuscript and approving it for publication was Gang Mei.

Flow cavitation in the nozzle-flapper servo valve may lead to noise, erosion, forced vibration and even instability [3], [9]–[11]. In the study of the nozzle-flapper pilot valve, Aung and Li [12] found that the curved surface of the traditional flapper may contribute to the formation of the flow cavitation and consequently a rectangular flapper is proposed to suppress flow cavitation. Yang *et al.* [13] further investigated the cavitation characteristics in the nozzle-flapper pilot valve using traditional flapper, rectangular flapper and square flapper, respectively. A detail comparison has been made among them. It is found that both the rectangular and square flappers could reduce the flow cavitation in the pilot valve. And the former one is more effective, due to the further decay of the radial flow under the effect of the longer flat surface. It should be pointed out that the replacement of the traditional flapper by the rectangular flapper may change some mechanical properties, e.g., forced deformation and natural frequency. This may affect the static and dynamic performance of the nozzle-flapper servo valve. Thus, further studies should be conducted to explore the novel strategies for cavitation suppression in servo valves.

The flow structure in the nozzle-flapper pilot stage can be identified as the combination of the impinging jet from nozzle and the radial jet from the clearance between the nozzle and the flapper. Thus, cavitation reduction may be achieved by jet manipulation, e.g., non-circular nozzles [14], tabs [15], plasma actuators [16], piezoelectric actuators [17], MEMS-based flap actuators [18], synthetic jets [19] and microjets [20], [21]. Based on this consideration, this work proposes a novel method of using diamond nozzles to reduce the flow cavitation in the nozzle-flapper pilot stage of a servo valve. The flow characteristics of the pilot stage are explored with computational fluid dynamics (CFD) software FLUENT, while the performance of the servo valve is simulated with AMESim. Section II presents a brief introduction of working principle of nozzle-flapper servo valve. CFD modeling of nozzle-flapper pilot stage is described in section III and experimental setup for CFD verification is shown in section IV. Section V presents the simulation of nozzle-flapper servo valve using AMESim. The results and discussions are shown in section VI, and the conclusions are summarized in section VII.

II. WORKING PRINCIPLE OF NOZZLE-FLAPPER SERVO VALVE

The structure of a typical nozzle-flapper servo valve is shown in Fig. 1. It consists of a torque motor, a nozzle-flapper stage and a spool stage. The torque motor includes two magnetic conductors, two permanent magnets, a flexure tube, an armature and coils intertwined on the armature. The nozzle-flapper stage consists of a flapper and twin nozzles while the spool stage includes a spool and a feedback spring. Initially, there are no electrical current in the coils, the flapper is placed at the same distance away from each nozzle. The oil flow in the left nozzle and corresponding upstream pipeline are equivalent to the counterparts on the right side, which results in a pressure
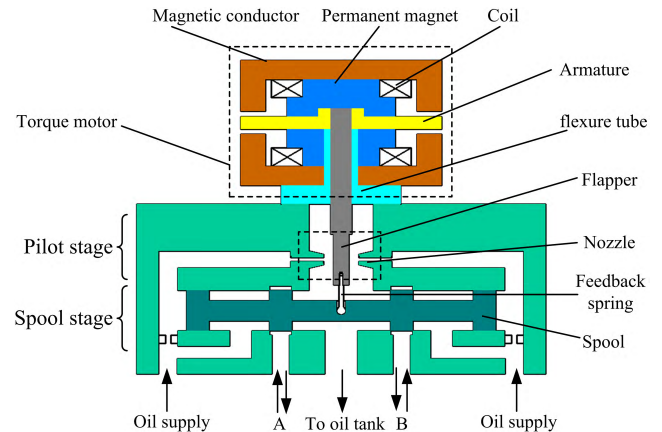

FIGURE 1. Schematic of nozzle-flapper servo valve.

balance at the left and right sides of the spool. As the coils are charged with the working current, a rotating torque is imposed on the armature under the electromagnetic field. The flapper fastened to the armature undergoes a rotation, approaching to one of the twin nozzles. This produces a pressure difference of the oil flow in the two nozzles and further at the two sides of the spool, leading to the movement of the spool. Finally, the total forces caused by the feedback spring, flexure tube, electromagnetic field and impinging jet issuing from each nozzle reach a balance state, the flapper returns to the initial position. As a result, the pressure balance at the both sides of the spool is recovered and the spool stops. The opening at the ports of the spool is proportional to the working current.

III. CFD MODELING OF NOZZLE-FLAPPER PILOT STAGE
A. 3D GEOMETRY
The three-dimensional (3D) CFD model of the nozzle-flapper pilot stage is presented in Fig. 2, along with the definitions of the cylindrical coordinates (x, θ, r) and the Cartesian coordinates (x, y, z). The surrounding wall has 3.5 mm in diameter and 8 mm in height. The diameter of the flapper is of 2 mm, and the distance between two parallel flat surfaces of the lower half is of 1.7 mm. The flapper has a distance of 0.1 mm away from each nozzle. The traditional nozzle has an inner diameter of 0.6 mm while the diamond nozzle has a side length of 0.53 mm, to ensure an equivalent area of the outlets. The structural parameters are summarized in Table 1.

B. GRID MESH AND BOUNDARY CONDITIONS
A quarter of the 3D model is chosen as the computational flow domain, as presented in Fig. 3. Grid mesh is conducted using GAMBIT 2.4.6. The boundary conditions are defined using FLUENT 6.3.23.

A mixed grid scheme of the hexahedral and tetrahedral cell is used for meshing. The structural and hexahedral cells are adopted for the meshing in the nozzle and the slot between the nozzle and the flapper while the tetrahedral cells are used for other regions. Ten grid layers are deployed within the slot,
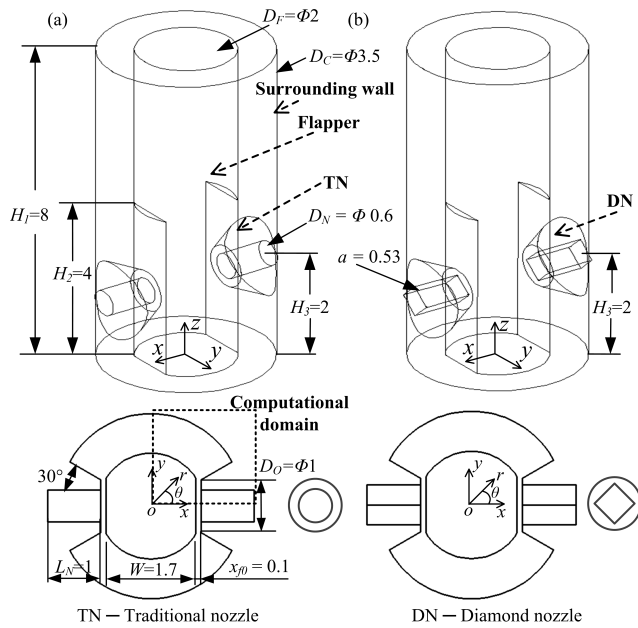
FIGURE 2. Flow model of the nozzle-flapper pilot stage (scale in mm). (a) Traditional nozzle, (b) Diamond nozzle.

TABLE 1. Structural parameters.

Symbol	Parameters	Value (mm)
H_1	chamber height	8
D_C	chamber inner diameter	3.5
D_F	flapper diameter	2
W	width of the lower part of the flapper	1.7
x_{f0}	null clearance between nozzle and flapper	0.1
D_N	inner diameter of the traditional nozzle	1
a	side length of the diamond nozzle	0.53
L_N	nozzle length	1
D_O	outer diameter of the nozzle	1
H_2	height of the nozzle flat surface	4
H_3	Displacement between the nozzle centerline and the chamber bottom	2

to ensure the accuracy. A fixed-typed size function is used for the generation of the tetrahedral grids. The cells with the skewness value under 0.6 account for 98% in total 3D elements, and the maximum skewness value of the cells is about 0.75, suggesting the mesh quality is acceptable [13]. The grid independence analysis has been conducted. The minimal grid size is 0.01 mm while the maximal grid size is 0.06 mm. The total grid number is 778253 and 843917 for the traditional nozzle and diamond nozzle, respectively.

Four types of the boundary conditions are set in the computational flow domain. The pressure-inlet condition is defined at the inlet of the nozzle while the pressure-outlet condition is used for the outlet of the flow domain. The inlet pressure varies from 3 MPa to 7MPa. The actual pressure of the outlet is in the range of 0~4MPa. Note that the cavitation in the flapper-nozzle servo valve could be intensified by reducing the outlet pressure. Thus, the outlet pressure for CFD modelling in this work is set as the gauge pressure to study the severe cavitation characteristics, as did in [12] and [13].
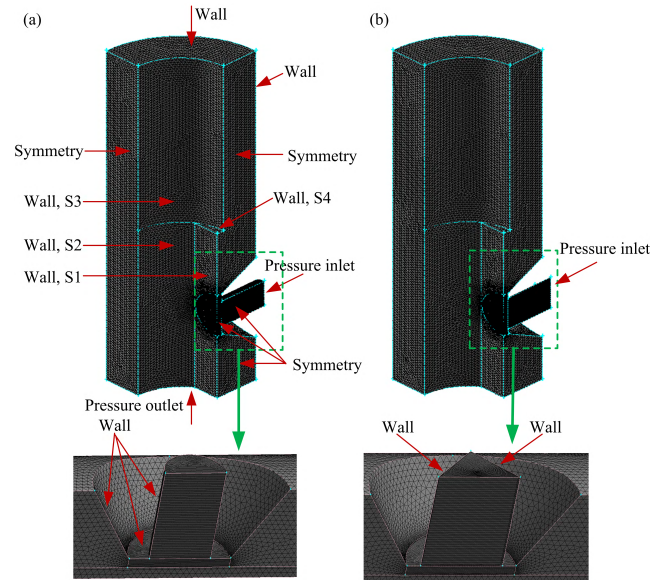

FIGURE 3. Boundary conditions and 3D grid mesh of the computational flow domain. (a) Traditional nozzle. (b) Diamond nozzle.

The symmetry-type condition is given for the symmetry planes, and the wall-type condition is applied for other surfaces.

C. GOVERNING EQUATIONS

Considering that Eulerian model is computationally consuming and explicit VOF model is not suitable for the cavitation modeling [22]–[24], a two-phase mixture model is adopted for studying flow cavitation in this work. A preliminary investigation shows that there is a negligible difference among the standard, RNG and Realizable k-ε models in predicting the mass flow rate. This is consistent with previous studies on the cavitating water hydraulic valves [7], [8], [25]. Thus, in this work, the Singhal *et al.* model is used for solving vapor fraction and the standard k-ε model is chosen for calculating turbulent characteristics, as used in [12], [13], and [26]–[28]. The governing equations include continuity equation, momentum equation, turbulent dissipation rate equation, turbulence kinetic energy equation and vapor transport equation.

Continuity equation:

$$\frac{\partial \rho_m}{\partial t} + \nabla \cdot \left(\rho_m \overrightarrow{u}_m \right) = 0 \tag{1}$$

where t is the time, ρ_m and $\overrightarrow{u}_m$ are the mixture density and velocity, respectively.

Momentum equation:

$$\begin{aligned}
\frac{\partial}{\partial t}(\rho_m \overrightarrow{u}_m) &+ \nabla \cdot (\rho_m \overrightarrow{u}_m \overrightarrow{u}_m) \\
&= -\nabla p + \nabla \cdot [\mu_m (\nabla \overrightarrow{u}_m + \nabla \overrightarrow{u}_m^T)] \\
&+ \rho_m \overrightarrow{g} + \overrightarrow{F} + \nabla \cdot (\sum_{k=1}^{n} \alpha_k \rho_k \overrightarrow{u}_{dr,k} \overrightarrow{u}_{dr,k})
\end{aligned} \tag{2}$$

where p is the pressure, μ_m is the mixture viscosity, $\overrightarrow{F}$ is the body force, $\overrightarrow{g}$ is the gravity, n is the phase number, $\overrightarrow{u}_{dr,k}$ is the drift velocity.

Turbulence kinetic energy equation and dissipation rate equation are given by:

$$\frac{\partial}{\partial t}(\rho_m k) + \nabla \cdot (\rho_m \overrightarrow{u}_m k)$$
$$= \nabla \cdot [(\mu + \frac{\mu_{t,m}}{\sigma_k})\nabla k] + G_{k,m} - \rho_m \varepsilon \qquad (3)$$

$$\frac{\partial}{\partial t}(\rho_m \varepsilon) + \nabla \cdot (\rho_m \overrightarrow{u}_m \varepsilon)$$
$$= \nabla \cdot [(\mu + \frac{\mu_{t,m}}{\sigma_\varepsilon})\nabla \varepsilon] + \frac{\varepsilon}{k}(C_{1\varepsilon}G_{k,m} - C_{2\varepsilon}\rho_m \varepsilon) \qquad (4)$$

where the turbulent viscosity of the mixture $\mu_{t,m}$ can be calculated by:

$$\mu_{t,m} = C_\mu \rho_m \frac{k^2}{\varepsilon} \qquad (5)$$

where $C_{1\varepsilon} = 1.44$, $C_{2\varepsilon} = 1.92$, $C_\mu = 0.09$, $\sigma_k = 1$ and $\sigma_\varepsilon = 1.3$ for the standard k-ε model.

Vapor transport equation:

$$\frac{\partial}{\partial t}(\rho_m f_v) + \nabla \cdot (\rho_m \overrightarrow{u}_v f_v) = \nabla(\gamma \nabla f_v) + R_e - R_c \qquad (6)$$

where f_v and $\overrightarrow{u}_v$ are the vapor mass fraction and velocity, respectively. γ is the diffusion coefficient. R_c and R_e denote the vapor condensation and generation rate, respectively. They are given in the Singhal et al. model as follows

$$R_c = C_c \frac{\sqrt{k}}{\sigma}\rho_l \rho_v \sqrt{\frac{2(p - p_v)}{3\rho_l}}(1 - f_v) \quad \text{if } p > p_v \qquad (7)$$

$$R_e = C_e \frac{\sqrt{k}}{\sigma}\rho_l \rho_v \sqrt{\frac{2(p_v - p)}{3\rho_l}}(1 - f_v - f_g) \text{ if } p \le p_v \qquad (8)$$

where $C_c = 0.01$ is the condensation rate coefficient, $C_e = 0.02$ is the vaporization rate coefficient, $f_g = 1.5 \times 10^{-5}$ is the non-condensable gas fraction. p_v is the phase-change threshold pressure, and it can be expressed as

$$p_v = p_{sat} + \frac{1}{2}p_t \qquad (9)$$

where $p_t = 0.39\rho k$ is turbulent pressure fluctuation, p_{sat} is vapor saturation pressure.

The governing equations are solved under steady conditions using commercial software FLUENT. The pressure-velocity coupling calculation is conducted using the SIMPLEC scheme. The PRESTO! algorithm and QUICK scheme are adopted for the pressure and vapor discretization, respectively. And the momentum, turbulent kinetic energy and turbulent dissipation rate terms are discretized with first order upwind algorithm. A converged solution of liquid flow is achieved before applying the cavitation model. The liquid density of hydraulic oil is 850 kg/m^3 and the liquid viscosity is 0.0085 Pa·s. The vaporization pressure of hydraulic oil is 3000 Pa and surface tension coefficient is 0.0273 N/m. The vapor density is 0.025 kg/m^3 and the vapor viscosity is 1×10^{-5} Pa·s.

IV. EXPERIMENTAL SETUP

The flow characteristics in the nozzle-flapper stage are experimentally investigated to verify the CFD simulation. Mass flow rate is one of the key parameters in hydraulic valves and it is convenient to be measured in hydraulic circuit. Thus, the mass flow rate measurement is used in this work for quantitatively verifying CFD modelling, as did in the studies of other hydraulic valves, e.g., [5], [7], [8]. On the other hand, the image observations of the flow field are also obtained to qualitatively validate the CFD simulation.
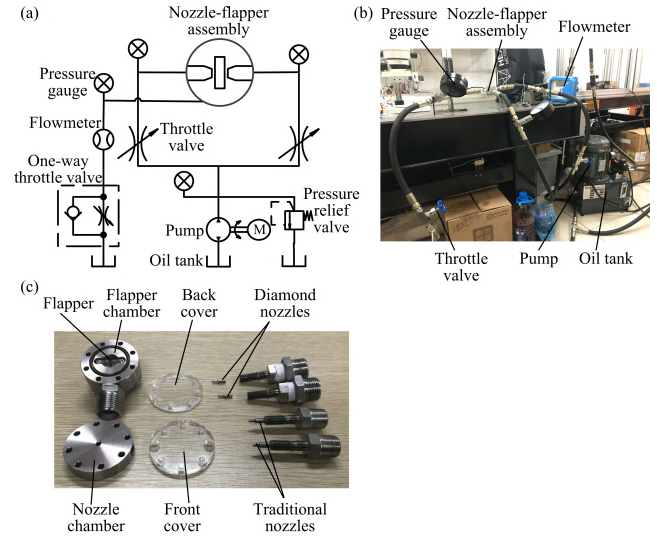

FIGURE 4. Experimental setup. (a) Hydraulic circuit. (b) Photograph of the test rig. (c) Nozzle-flapper assembly.

The experimental setup consists of hydraulic pump, pipeline, throttle valves, pressure gauges, nozzle-flapper assembly, flowmeter and oil tank, as shown in Fig. 4(a-b). The hydraulic oil is supplied by a hydraulic pump. The rated pressure of the hydraulic pump is 21 MPa and corresponding flow rate is 2.9 L/min. The pressure is adjusted by three throttle valves and measured by three pressure gauges with an accuracy of ±1.6%. Two pressure gauges with a measuring range of 0 – 16 MPa are placed at the upstream of the nozzle-flapper assembly while one pressure gauge with a range of 0 – 1 MPa is installed at the downstream. The flow rate is measured by a flowmeter placed at the downstream of the nozzle-flapper assembly. The flowmeter has a measuring range of 0 – 150 L/h and an accuracy of ±1.5%. A digital microscope is deployed to capture the flow field.

The nozzle-flapper assembly consists of a flapper, a flapper base, a flapper chamber, a back cover, a front cover, two nozzles and a nozzle chamber (Fig. 4c). The flapper is installed in the flapper chamber through the flapper base. The components of the assembly are fabricated by Computer Numerical Control (CNC) machines and the fabrication error is under 0.02 mm. The material of the nozzles is stainless steel. The smallest round and diamond holes in the nozzles are fabricated through wire cut electrical discharge machining with low wire travelling speed (WEDM-LS). The traditional

nozzles are placed in the nozzle chamber through the screw thread connections. The diamond nozzles are installed in the nozzle chamber through a strong adhesive. The distance between the two nozzles is set to 1.9 mm. A square cylinder with a dimension of 1.9 mm × 1.9 mm is inserted into the gap between the two nozzles, to assist the distance adjustment. The experimental error mainly comes from the fabrication imperfection, the measurement accuracy of the flowmeter and that of the pressure gauges.

V. SIMULATION ON NOZZLE-FLAPPER SERVO VALVE

To explore the effect of the diamond nozzles on the static and dynamic performance of the nozzle-flapper servo valve, the pressure-flow characteristics and the load flow rate under a step of current are examined using AMESim simulation.
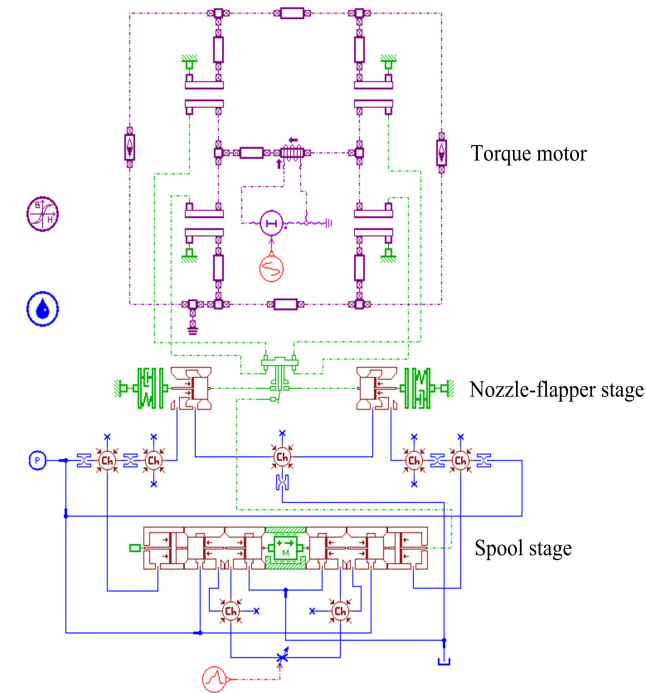

FIGURE 5. Simulation diagram of nozzle-flapper servo valve in AMESim.

Based on the working principle of the nozzle-flapper servo valve, a simulation model can be established, as presented in Fig. 5. It consists of torque-motor model, nozzle-flapper model and spool model. The torque-motor model includes coil, magnetic elements, magnetic air gaps, permanent magnets, magnetic junctions, and current source. The nozzle-flapper stage model mainly consists of armature-flapper and nozzle-flappers and elastic contacts. The spool stage model includes pistons, spools with rounded edges and annular section orifice, mass with friction and configurable end stops, hydraulic chamber with variable volume and pressure dynamics, variable hydraulic orifice, hydraulic tank, and hydraulic pressure source.

In this work, the diamond nozzles are deployed to replace the traditional nozzle, the flow forces on the flapper exhibit

a slight change. Thus, the nozzle-flapper model needs to be modified while the torque-motor model and spool model remain. The flow forces upon the flapper for the traditional nozzle and the diamond nozzle can be obtained by CFD modeling, their relation can be expressed as

$$F_{\text{D}} = \lambda F_{\text{T}} \tag{10}$$

where F_D and F_T are the flow force on the flapper for the diamond nozzle and the traditional nozzle, respectively. λ is the coefficient, which is then used for modifying the structural parameter in AMESim model.

In AMESim simulation model, the flow forces upon the flapper can be described by the following equation [29]

$$F = p_1 \frac{\pi}{4} D_N^2 + p_0 \frac{\pi}{4} (D_f^2 - D_N^2) \tag{11}$$

where F is the flow force on the flapper by the flow impingement from each nozzle, p_1 is the pressure at the inlet of the nozzle, p_0 is the discharged pressure, D_N is the internal diameter of the nozzle, D_f is the diameter of the flapper.

Based on (10) and (11), the equivalent internal diameter of the nozzle D_{ND} and the equivalent diameter of the flapper D_{fD} for the case of the diamond nozzle can be given as

$$D_{ND} = \sqrt{\lambda} D_{NT}, \quad D_{fD} = \sqrt{\lambda} D_{fT} \tag{12}$$

where D_{NT} and D_{fD} denote the internal diameter of the nozzle and the diameter of the flapper for the case of the traditional nozzle, respectively.

In the simulation, the supplied pressure P_s adopted is of 21 MPa and the input current I is set to −0.01 A, −0.005 A, 0 A, 0.005 A, 0.01 A, respectively. The time interval and duration are 0.001 s and 10 s in the simulation of static characteristics while those are 0.0001 s and 0.04 s in the simulation of dynamic characteristics, respectively.

VI. RESULTS AND DISCUSSIONS
A. FLOW CHARACTERISTICS OF THE NOZZLE-FLAPPER PILOT STAGE
1) MASS FLOW RATE

In the flapper-nozzle servo valve, mass flow rate of the pilot stage determines the leakage loss coefficient of the servo valve. Fig. 6 presents the numerical and experimental mass flow rates of the outlet in the pilot stage. The inlet pressure is varied from 3 to 8 MPa. In the pilot stage with traditional nozzles, the averaged relative derivation between numerical and experimental results is of 5.57%. In the pilot stage with diamond nozzles, the mean relative departure between numerical and experimental results is of 6.63%. This indicates that numerical mass flow rates exhibit a good agreement with experimental results. In other words, the CFD modelling is appropriate to explore the flow characteristics of the flapper-nozzle pilot valve. Moreover, compared with mass flow rates in case of traditional nozzles, those in case of diamond nozzles exhibit a slight averaged increase of 3.72% and 2.69% for CFD and experimental results, respectively. This suggests that the diamond nozzles have a negligible effect on the mass flow rates.
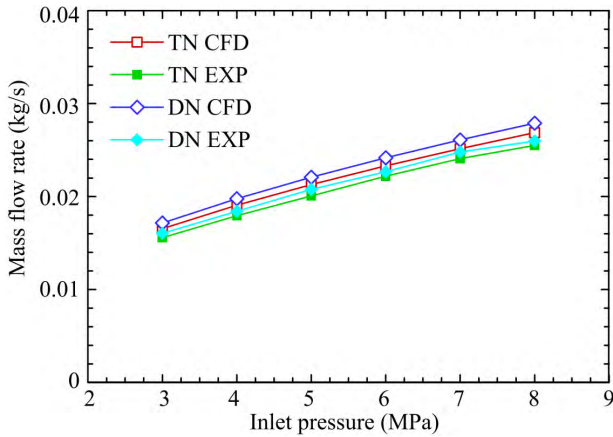
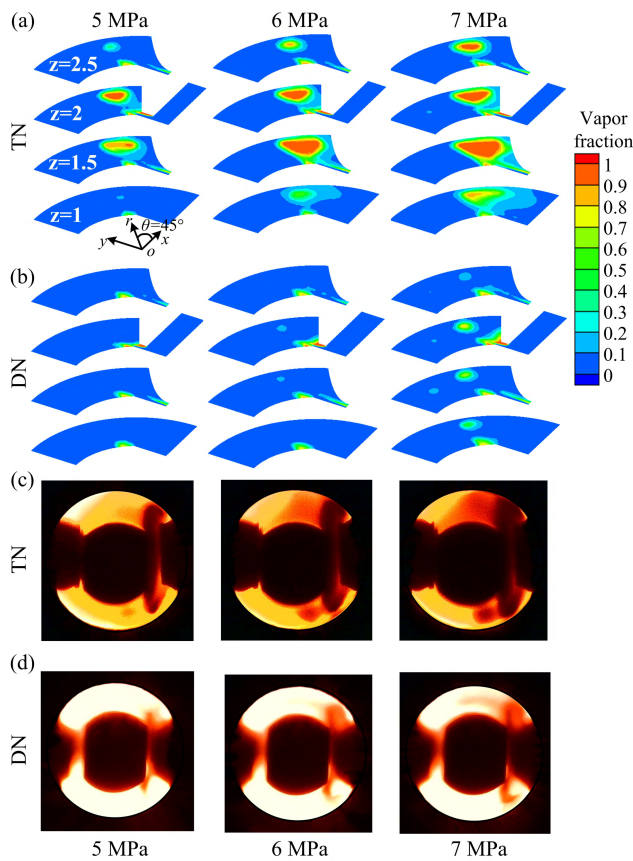**FIGURE 6.** Mass flow rate of the outlet of the nozzle-flapper pilot stage.

FIGURE 7. Comparison of cavitation phenomenon between traditional nozzle and diamond nozzle. (a-b) Vapor fraction contours obtained from CFD modelling. (c-d) Experimental photographs.

2) VAPOR FRACTION

To explore the cavitation suppression in detail, vapor fraction is examined in a series of orthogonal planes, i.e., the planes at $z = 1 - 2.5$ mm and $\theta = 45°$, respectively. The former ones are parallel to the chamber bottom while the latter one cuts through the vapor area in the former ones.

Fig. 7 presents the vapor fraction contours in the cross-sectional planes of $z = 1, 1.5, 2, 2.5$ mm. The plane of $z = 2$ mm is crossing through the nozzle centerline. In the pilot

stage with traditional nozzles, the vapor occurs on the curved surface of the flapper, the nozzle tip, and the corner between the surrounding wall and the nozzle. At the inlet pressure $P_{in} = 5$ MPa, a small amount of vapor is present in the planes of $z = 1$ and 2.5 mm while a large amount of vapor occurs in the planes of $z = 1.5$ and 2 mm. Note that the vapor mainly emerges in the corner between the surrounding wall and the nozzle. As P_{in} rises to 7MPa, the area of the vapor rises to cover the whole corner in the planes of $z = 1.5$ and 2 mm, and exhibits a remarkable increase in the planes of $z = 1$ and 2.5 mm. This indicates that flow cavitation is strongly enhanced with the increase of the inlet pressure. This is consistent with the experimental observations in [13]. In the pilot stage with diamond nozzles, the vapor fraction is evidently reduced, especially in the corner between the surrounding wall and the nozzle. At the inlet pressure $P_{in} = 5$ MPa, the vapor fraction is absent in the corner. As P_{in} rises to 7MPa, the vapor area is extended along the nozzle edge and emerges in the region between the surrounding wall and the flapper. In spite of this, the vapor fraction is greatly reduced, compared to that for the traditional nozzle.

The experimental photographs of the flow field are also given in Fig. 7. It should be noted that the experimental photographs are affected by low visibility of the hydraulic fluid and imperfectness in fabrication. In this work, the hydraulic oil is only injected from one nozzle, to increase the visibility. Two observations can be made. Firstly, the experimental photographs exhibit a good agreement with numerical results in the plane of $z = 2$ mm. This also suggests that the simulation setup is reasonable for the modelling of the pilot stage. Secondly, the cavitation becomes intensified with the increase of the inlet pressure for both the traditional nozzle and the diamond nozzle. However, the cavitation is noticeably suppressed by the diamond nozzle.
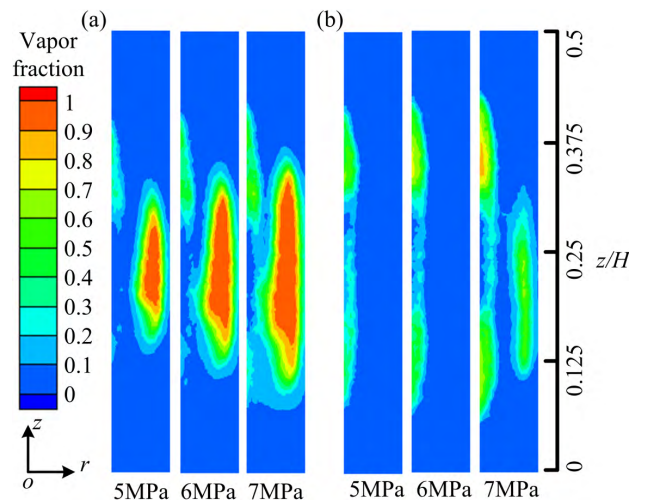

FIGURE 8. Vapor fraction contours in the plane of $\theta = 45°$. (a) Traditional nozzle. (b) Diamond nozzle.

Fig. 8 shows the vapor fraction contours in the plane of $\theta = 45°$. In the pilot stage with traditional nozzles, the vapor is evident on the flapper surface and the region between

the surrounding wall and the flapper surface. Note that the predominant region along z direction that the vapor occurs is that around the nozzle. As the inlet pressure goes up from 5 MPa to 7 MPa, the vapor area is greatly enlarged. In the pilot stage with diamond nozzle, the vapor fraction in the region between the surrounding wall and the flapper surface is reduced while that on the flapper surface is slightly enhanced. At $P_{in} = 5$ MPa and 6 MPa, the vapor is absent in the region between the surrounding wall and the flapper surface. Further at $P_{in} = 7$ MPa, the vapor in this area is still strongly reduced. This indicates that the diamond nozzles are effective on the suppression of the vapor in the region between the surrounding wall and the flapper surface.

3) FLOW VELOCITY

To explore the physical mechanism behind cavitation suppression, flow velocity is examined in a series of orthogonal planes, i.e., the planes at $z = 1 - 2.5$ mm and $x = -0.9$ mm, respectively. The former ones are parallel to the chamber bottom while the latter one cuts through the centerline of the clearance between the flapper and the nozzle.
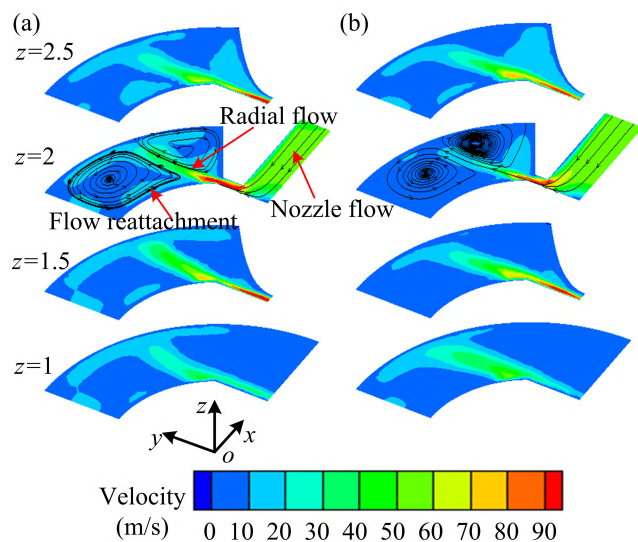

FIGURE 9. Streamlines and velocity contours in the planes of **z = 1, 1.5, 2, 2.5 mm at P_{in} = 6 MPa. (a) Traditional nozzle. (b) Diamond nozzle.**

Fig. 9 shows the streamlines and the velocity contours in the planes of $z = 1, 1.5, 2, 2.5$ mm. The plane of $z = 2$ mm is crossing through the nozzle centerline. In the pilot stage with the traditional nozzles, the flow structure can be identified as the combination of the nozzle flow, the radial flow and the flow reattachment. This is consistent with previous study by Aung *et al.* [27]. Initially, the nozzle flow from the inlet impinges upon the flat wall of the flapper. After that, the flow deflects along the clearance between the flapper and the nozzle, forming a radial jet. Then, the radial jet flow impinges upon the surrounding wall and turns to move along the wall. Finally, the flow reattaches to the beveled wall of the nozzle and the curved surface of the flapper, producing flow structures with a clockwise and anti-clockwise rotation,

respectively. Note that the radial jet velocity decreases and the flow reattachment becomes weakened in the planes of $z = 1$, 1.5, 2.5 mm that are away from the nozzle. Apparently, this is due to that the jet flow decays as it moves downstream [20]. In the pilot stage with the diamond nozzles, the velocity of the radial flow exhibits a remarkable drop, especially in the plane of $z = 2$ mm. As a result, the impingement upon the surrounding wall and consequent flow reattachment are suppressed. Thus, the reduced velocity of the radial flow may be responsible for the reduction of the vapor fraction. In the study of the cavitation reduction in nozzle-flapper pilot valve using a rectangle-shaped flapper, Yang *et al.* [13] also confirmed that the cavitation reduction is due to the reduced strength of radial jet flow by longer flat surface of the rectangle-shape flapper.
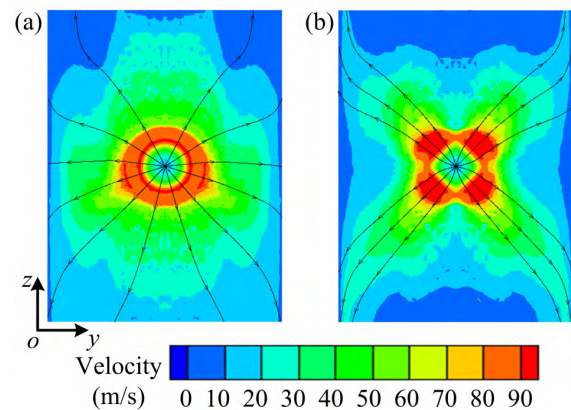

FIGURE 10. Streamlines and velocity contours in the plane of **x = 0.9 mm at P_{in} = 6 MPa. (a) Traditional nozzle. (b) Diamond nozzle.**

Fig. 10 presents the streamlines and the velocity contours in the plane of $x = -0.9$ mm. In the pilot stage with the traditional nozzles, the flow is roughly along the normal directions of the nozzle perimeter, especially in the central region of this plane. In contrast, the flow in case of diamond nozzles is mainly along the normal directions of the diamond edges. Only a small amount of the flow moves along the diagonal directions of the diamond nozzle. This is consistent with the flow structure in the square impinging jet at small ratio of plate distance to nozzle equivalent diameter, that is, the jet flow spreads along the normal directions of four square edges [30]. This flow structure leads to a rapid decay of the flow velocity along y-axis, which is responsible for the reduced radial velocity shown in the plane of $z = 2$ mm (Fig. 9). Thus, the flow structure of the diamond impinging jet attributes to the cavitation reduction in the region between the surrounding wall and the flapper surface (Fig. 8).

4) PRESSURE DISTRIBUTION

The static pressure distributions on the flapper surfaces are compared between the pilot stage with the traditional nozzles and that with the diamond nozzles, as shown in Fig. 11. It can be observed that the pressure distributions are qualitatively the same for both cases, except for the region around the
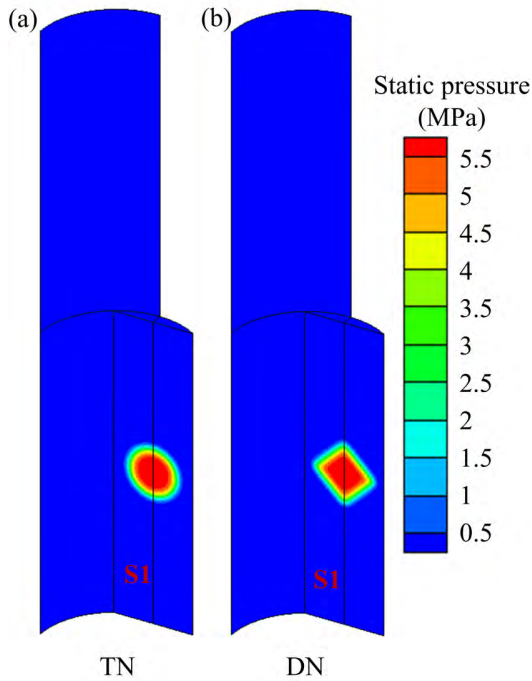
FIGURE 11. Static pressure contours on the flapper surfaces at P_{in} = 6 MPa. (a) Traditional nozzle. (b) Diamond nozzle.
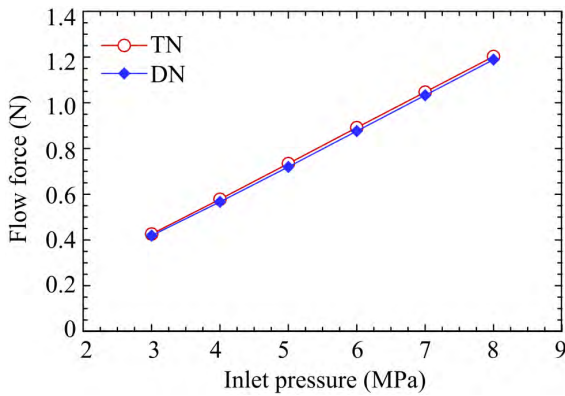

FIGURE 12. Flow force on the flapper surface S1.

nozzle. In the pilot stage with the traditional nozzles, the distribution of the static pressure on the flapper surface S1 is in a round shape. In contrast, the pressure distribution for the case of diamond nozzles presents a diamond shape. This is apparently due to the impingement difference between the round jet and the diamond jet.

5) FLOW FORCES

In the nozzle-flapper servo valve, the flow forces on the flapper directly determine the flapper deflection [9] and thus they are of great importance to the performance of the servo valve. Since the pressure distributions on the flapper surfaces mainly concentrate around the nozzles (Fig. 11), the flow forces on the flapper surface S1 is the main concern.

Fig. 12 compares the flow forces on the flapper surface S1 between the pilot stage with the traditional nozzles and that with the diamond nozzles. Two observations cam
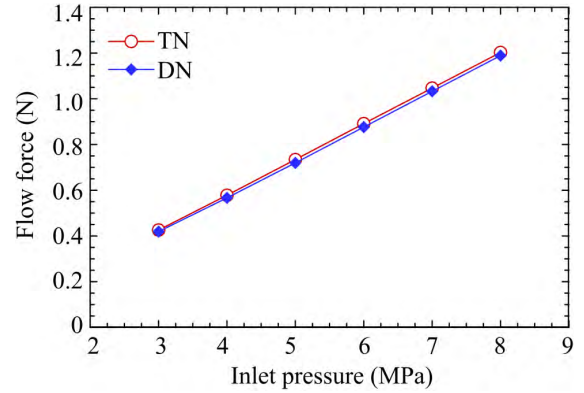

FIGURE 13. Dependence of load flow rate on load pressure drop under different input current.
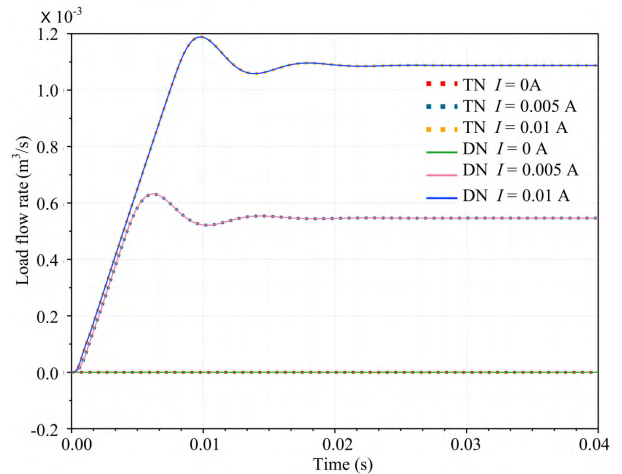

FIGURE 14. Time step response of the load flow rate under different input current.

be made. Firstly, the variation of the flow forces with the increase of the inlet pressure is qualitatively the same for both cases, exhibiting a roughly linear rising trend. Secondly, the flow forces in case of diamond nozzles are slightly smaller than those in case of the traditional nozzles, the mean departure of the flow forces between two cases is of 1.6%. Thus, the diamond nozzles have a negligible effect on the force forces on the flapper surface S1. This may indicate that the diamond nozzles could suppress the flow cavitation without changing the main force characteristics of the servo valve.

B. PERFORMANCE OF THE NOZZLE-FLAPPER SERVO VALVE

To further explore the effect of the diamond nozzles on the performance of the nozzle-flapper servo valve, the pressure-flow characteristics and time step response of the load flow rate are explored using the AMESim simulation. The former one represents the static performance of the nozzle-flapper servo valve while the latter one denotes the dynamic performance of the servo valve.

Fig. 13 presents the relation between load flow rate and load pressure drop under different input currents while Fig. 14 shows the time response of load flow rate under

step input currents. Two observations can be made. Firstly, the curves for both traditional nozzles and diamond nozzles almost overlap for each current. This indicates that the pressure-flow characteristics remain the same under the effect of the diamond nozzles. Secondly, the time step response of the load flow rate exhibits a neglectable variation between the traditional nozzles and the diamond nozzles. This suggests that the diamond nozzles have little effect on the dynamic response of the controlled flow rate. Thus, diamond nozzles could reduce flow cavitation without changing the static and dynamic performance of the nozzle-flapper servo valve.

VII. CONCLUSIONS

In this work, diamond nozzles are proposed to suppress the flow cavitation in the nozzle-flapper pilot stage of a servo valve. Flow characteristics in the pilot stage are investigated using ANSYS/FLUENT and verified by mass flow rate and image measurement, while the effect of the diamond nozzles on the performance of the servo valve is numerically studied using AMESim. The following conclusions may be made from this work.

1) The vapor fraction in the pilot stage with the diamond nozzles is significantly reduced, compared to that in the traditional pilot stage. This indicates that diamond nozzle could effectively suppress the flow cavitation.

2) In the pilot stage with the traditional round nozzles, the flow moves along the normal directions of the nozzle perimeter after impinging upon the flapper surface. In contrast, the impinging flow in case of the diamond nozzles mainly turns to move along the normal directions of the diamond edges. As a result, the flow along the diagonal direction of the diamond nozzle undergoes a rapid decay, which suppresses the impingement of the radial flow upon the surrounding wall. Thus, the flow structure of the diamond impinging flow is responsible for the cavitation reduction.

3) The mass flow rate and the flow forces upon the flapper in the pilot stage with diamond nozzles varied slightly, compared to those in case of traditional nozzle. This may suggest that the diamond nozzles have a little effect on the leakage loss coefficient and the force characteristics of the servo valve.

4) The pressure-flow characteristics and time step response of the load flow rate exhibit a neglectable variation between the traditional nozzles and the diamond nozzles. This indicates that the diamond nozzles could reduce flow cavitation without changing the static and dynamic performance of the nozzle-flapper servo valve.

Thus, this work proposes a novel method of using diamond nozzles to reduce the flow cavitation in the nozzle-flapper pilot stage of a servo valve. Numerical investigations have been conducted using CFD modelling and AMESim. It is shown that the cavitation could be greatly reduced without affecting the performance of the servo valve, e.g., the pressure-flow characteristics, time step response of the load

flow rate and energy loss indicated by the mass flow rate of the pilot stage. However, further studies are required to investigate cavitation phenomenon under transient operation of the nozzle and experimentally explore the performance of the servo valves which are implemented the diamond nozzles.

REFERENCES

[1] X. Yang, X. Zheng, and Y. Chen, "Position tracking control law for an electro-hydraulic servo system based on backstepping and extended differentiator," *IEEE/ASME Trans. Mechatronics*, vol. 23, no. 1, pp. 132–140, Feb. 2018.

[2] C. Wang, Z. Jiao, S. Wu, and Y. Shang, "Nonlinear adaptive torque control of electro-hydraulic load system with external active motion disturbance," *Mechatronics*, vol. 24, no. 1, pp. 32–40, Feb. 2014.

[3] M. Chen, D. Xiang, S. Li, and C. Zou, "Suppression of squeal noise excited by the pressure pulsation from the flapper-nozzle valve inside a hydraulic energy system," *Energies*, vol. 11, no. 4, p. 955, 2018.

[4] W. Zhang, J. Peng, and S. Li, "Damping force modeling and suppression of self-excited vibration due to magnetic fluids applied in the torque motor of a hydraulic servovalve," *Energies*, vol. 10, no. 6, p. 749, 2017.

[5] R. Amirante, E. Distaso, and P. Tamburrano, "Experimental and numerical analysis of cavitation in hydraulic proportional directional valves," *Energy Convers. Manage.*, vol. 87, pp. 208–219, Nov. 2014.

[6] J. Zou *et al.*, "Cavitation in a non-circular opening spool valve with U-grooves," *Proc. Inst. Mech. Eng., A, J. Power Energy*, vol. 222, pp. 413–420, Jun. 2008.

[7] M. Han, Y. Liu, D. Wu, X. Zhao, and H. Tan, "A numerical investigation in characteristics of flow force under cavitation state inside the water hydraulic poppet valves," *Int. J. Heat Mass Transf.*, vol. 111, pp. 1–16, Aug. 2017.

[8] J. Liang, X. Luo, Y. Liu, X. Li, and T. Shi, "A numerical investigation in effects of inlet pressure fluctuations on the flow and cavitation characteristics inside water hydraulic poppet valves," *Int. J. Heat Mass Transf.*, vol. 103, pp. 684–700, Dec. 2016.

[9] L. Li, H. Yan, H. Zhang, and J. Li, "Numerical simulation and experimental research of the flow force and forced vibration in the nozzle-flapper valve," *Mech. Syst. Signal Process.*, vol. 99, pp. 550–566, Jan. 2018.

[10] M. Chen, N. Z. Aung, S. Li, and C. Zou, "Effect of oil viscosity on self-excited noise production inside the pilot stage of a two-stage electrohydraulic servovalve," *J. Fluids Eng.*, vol. 141, no. 1, p. 011106, 2018.

[11] S. Zhang and S. Li, "Cavity shedding dynamics in a flapper–nozzle pilot stage of an electro-hydraulic servo-valve: Experiments and numerical study," *Energy Convers. Manage.*, vol. 100, pp. 370–379, Aug. 2015.

[12] N. Z. Aung and S. Li, "A numerical study of cavitation phenomenon in a flapper–nozzle pilot stage of an electrohydraulic servo-valve with an innovative flapper shape," *Energy Convers. Manage.*, vol. 77, pp. 31–39, Jan. 2014.

[13] Q. Yang, N. Z. Aung, and S. Li, "Confirmation on the effectiveness of rectangle-shaped flapper in reducing cavitation in flapper–nozzle pilot valve," *Energy Convers. Manage.*, vol. 98, pp. 184–198, Jul. 2015.

[14] E. J. Gutmark and F. F. Grinstein, "Flow control with noncircular jets," *Annu. Rev. Fluid Mech.*, vol. 31, no. 1, pp. 239–272, 1999.

[15] M. F. Reeder and M. Samimy, "The evolution of a jet with vortex-generating tabs: Real-time visualization and quantitative measurements," *J. Fluid Mech.*, vol. 311, pp. 73–118, Mar. 1996.

[16] T. C. Corke, C. L. Enloe, and S. P. Wilkinson, "Dielectric barrier discharge plasma actuators for flow control," *Annu. Rev. Fluid Mech.*, vol. 42, pp. 505–529, Sep. 2010.

[17] J. M. Wiltse and A. Glezer, "Manipulation of free shear flows using piezoelectric actuators," *J. Fluid Mech.*, vol. 249, pp. 261–285, Apr. 1993.

[18] L. N. Cattafesta and M. Sheplak, "Actuators for active flow control," *Annu. Rev. Fluid Mech.*, vol. 43, pp. 247–272, Jan. 2011.

[19] A. Glezer and M. Amitay, "Synthetic jets," *Annu. Rev. Fluid Mech.*, vol. 34, no. 1, pp. 503–529, 2002.

[20] H. Yang and Y. Zhou, "Axisymmetric jet manipulated using two unsteady minijets," *J. Fluid Mech.*, vol. 808, pp. 362–396, Dec. 2016.

[21] H. Yang, Y. Zhou, R. M. C. So, and Y. Liu, "Turbulent jet manipulation using two unsteady azimuthally separated radial minijets," *Proc. Roy. Soc. A, Math. Phys. Eng. Sci.*, vol. 472, no. 2191, Jul. 2016, Art. no. 20160417.

[22] R. Xue, Y. X. Ruan, X. F. Liu, L. Chen, and Y. Hou, "Numerical study of liquid nitrogen cavitating flow through nozzles of various shapes," *Cryogenics*, vol. 94, pp. 62–78, Sep. 2018.

[23] Y. X. Ruan *et al.*, "Effects of operational parameters on liquid nitrogen spray cooling," *Appl. Therm. Eng.*, vol. 146, pp. 85–91, Jan. 2019.

[24] R. Xue *et al.*, "Experimental study of liquid nitrogen spray characteristics in atmospheric environment," *Appl. Therm. Eng.*, vol. 142, pp. 717–722, Sep. 2018.

[25] M. Han, Y. Liu, D. Wu, H. Tan, and C. Li, "Numerical analysis and optimisation of the flow Forces in a water hydraulic proportional cartridge valve for injection system," *IEEE Access*, vol. 6, pp. 10392–10401, 2018.

[26] S. Zhang, N. Z. Aung, and S. Li, "Reduction of undesired lateral forces acting on the flapper of a flapper–nozzle pilot valve by using an innovative flapper shape," *Energy Convers. Manage.*, vol. 106, pp. 835–848, Dec. 2015.

[27] N. Z. Aung, Q. Yang, M. Chen, and S. Li, "CFD analysis of flow forces and energy loss characteristics in a flapper–nozzle pilot valve with different null clearances," *Energy Convers. Manage.*, vol. 83, pp. 284–295, Jul. 2014.

[28] S. Li, N. Z. Aung, S. Zhang, J. Cao, and X. Xue, "Experimental and numerical investigation of cavitation phenomenon in flapper–nozzle pilot stage of an electrohydraulic servo-valve," *Comput. Fluids*, vol. 88, pp. 590–598, Dec. 2013.

[29] C. Liu and H. Jiang, "A seventh-order model for dynamic response of an electro-hydraulic servo valve," *Chin. J. Aeronaut.*, vol. 27, no. 6, pp. 1605–1611, 2014.

[30] H. C. Meena, S. A. Reodikar, R. Vinze, and S. V. Prabhu, "Influence of the shape of the orifice on the local heat transfer distribution between smooth flat surface and impinging incompressible air jet," *Experim. Therm. Fluid Sci.*, vol. 70, pp. 292–306, Jan. 2016.

WEN WANG was born in 1968. He received the M.S. and Ph.D. degrees in mechanical engineering from Zhejiang University, Hangzhou, China, in 1992 and 1996, respectively, where he was a Lecturer with the School of Mechanical Engineering, from 1996 to 1998, and an Associate Professor, from 1998 to 2012.

From 2009 to 2010, he was a Visiting Scholar with the Center for Precision Metrology, University of North Carolina at Charlotte. Since 2012, he has been a Professor with the School of Mechanical Engineering, Hangzhou Dianzi University. He is the author of one book, over 100 articles, and over 70 patents. His research interests include micro/nano drives, sensors and actuators, precision measurement and control, coordinate measuring machines, and mechatronics equipment.

Dr. Wang is a Senior Member of the Chinese Mechanical Engineering Society, the Director of the Mechanical Dynamics Branch, Chinese Society of Vibration Engineering, and a Committee Member of the Geometric Measurement and Online Detection Technology Branch, Chinese Society of Measurement.

HE YANG was born in 1988. He received the B.S. and M.S. degrees in mechatronics engineering and the Ph.D. degree in fluid machinery and engineering from the Harbin Institute of Technology, Harbin, China, in 2010, 2012, and 2017, respectively.

From 2013 to 2014, he was a Research Assistant with the Department of Mechanical Engineering, The Hong Kong Polytechnic University, Hong Kong. Since 2017, he has been a Lecturer with the School of Mechanical Engineering, Hangzhou Dianzi University. His research interests include computational fluid dynamics, experimental fluid dynamics, electro-hydraulic control systems and components, sensors and actuators, jet flow, and microfluidics.

KEQING LU was born in 1980. He received the Ph.D. degree in mechanical engineering from Zhejiang University, Hangzhou, China, in 2010, where he was a Postdoctoral Researcher with the School of Mechanical Engineering, from 2010 to 2013.

After that, he was a Lecturer with the School of Mechanical Engineering, Hangzhou Dianzi University, where he has been an Associate Professor, since 2016. His research interests include precision measurement, CAD modeling of reverse engineering, digital measurement of complex surfaces, sensors, and actuators.

• • •